

PICS: SIMULATIONS OF STRONG GRAVITATIONAL LENSING IN GALAXY CLUSTERS

NAN LI^{1,2,3}; MICHAEL D. GLADDERS^{1,3}; ESTEBAN M. RANGEL^{2,5}; MICHAEL K. FLORIAN^{1,3};
 LINDSEY E. BLEEM^{2,3}; KATRIN HEITMANN^{2,3}; SALMAN HABIB^{2,3}, AND PATRICIA FASEL⁴

Preparing to submit to to ApJ: draft date June 16, 2022

ABSTRACT

Gravitational lensing has become one of the most powerful tools available for investigating the ‘dark side’ of the universe. Cosmological strong gravitational lensing, in particular, probes the properties of the dense cores of dark matter halos over decades in mass and offers the opportunity to study the distant universe at flux levels and spatial resolutions otherwise unavailable. Studies of strongly-lensed variable sources offer yet further scientific opportunities. One of the challenges in realizing the potential of strong lensing is to understand the statistical context of both the individual systems that receive extensive follow-up study, as well as that of the larger samples of strong lenses that are now emerging from survey efforts. Motivated by these challenges, we have developed an image-simulation pipeline, PICS (Pipeline for Images of Cosmological Strong lensing) to generate realistic strong gravitational lensing signals from group- and cluster-scale lenses. PICS uses a low-noise and unbiased density estimator based on (resampled) Delaunay Tessellations to calculate the density field; lensed images are produced by ray-tracing images of actual galaxies from deep Hubble Space Telescope observations. Other galaxies, similarly sampled, are added to fill in the light cone. The pipeline further adds cluster-member galaxies and foreground stars into the lensed images. The entire image ensemble is then observed using a realistic point spread function which includes appropriate detector artifacts for bright stars. Noise is further added, including such non-Gaussian elements as noise window-paning from mosaiced observations, residual bad pixels, and cosmic rays. The aim is to produce simulated images that appear identical—to the eye (expert or otherwise)—to real observations in various imaging surveys.

Subject headings: galaxies: clusters: dark matter—gravitational lensing: strong—methods : simulations

1. INTRODUCTION

Gravitational lensing is, put simply, the deflection of photon paths when they pass through a gravitational potential. In recent years, gravitational lensing has come to the fore as a powerful tool to investigate the “dark side” of the Universe (for reviews, see e.g., Massey et al. 2010; Kneib & Natarajan 2011; Treu et al. 2013; Meneghetti et al. 2013, and references therein). Lensing effects can be observed over a wide range of scales: from megaparsecs (weak lensing, Massey et al. 2007; Hoekstra & Jain 2008; Okabe et al. 2010; van Engelen et al. 2012; Mandelbaum et al. 2013; Kilbinger et al. 2013), to kilo parsecs (strong lensing, Treu 2010; Suyu et al. 2010; Oguri et al. 2012; Coe et al. 2013; Newman et al. 2013; Kelly et al. 2014), down to parsec scales (micro lensing Muraki et al. 2011; Mao 2012; Han et al. 2013; Gould & Yee 2014). It has been widely applied in extragalactic astrophysics and cosmology, e.g., in reconstructing the mass distributions of lenses (Mandelbaum et al. 2006; Umetsu & Broadhurst 2008; Oguri et al. 2012; Newman et al. 2013; Han et al. 2015), detecting galaxies

at high redshift (Richard et al. 2008; Jones et al. 2010, 2013; Stark et al. 2014), measuring the Hubble constant (Paraficz & Hjorth 2010; Suyu et al. 2013, 2014; Liao et al. 2015), amongst other applications.

Cosmological strong lensing is an extreme manifestation of this process, in which the mass density creating the potential—i.e., the lens, which is typically a massive galaxy or a group or cluster of galaxies—is sufficient to create multiple highly magnified and distorted images of background sources. The occurrence and morphological properties of these lensed images reflect both the properties of the gravitational potential between the source and the observer, and the lensing geometry. It is a powerful probe of the central mass structure in galaxy clusters and groups and offers unique constraints on such systems (Halkola et al. 2006; Sand et al. 2008; Newman et al. 2009; Limousin et al. 2010; Newman et al. 2011; Limousin et al. 2012; Bhattacharya et al. 2013; Grillo et al. 2015). Gravitational lensed arcs are used in a variety of cosmological applications (Kneib & Natarajan 2011; Meneghetti et al. 2013). The frequency of strongly lensed arcs on the sky reflects the abundance (Dalal et al. 2004; Li et al. 2006; Fedeli et al. 2007; Hilbert et al. 2007; Fedeli et al. 2010), the concentration (Oguri et al. 2012; Sereno & Covone 2013; Meneghetti et al. 2014) and astrophysical properties (Peter et al. 2013; Rozo et al. 2008) of massive lenses, and the redshift distribution and properties of the sources (Wambsganss et al. 2004; Bayliss et al. 2011a; Bayliss 2012). Thus, arc statistics help trace structure formation and can in principle provide constraints on cosmological parameters.

¹ Department of Astronomy & Astrophysics, The University of Chicago, 5640 South Ellis Avenue, Chicago, IL 60637, USA; linan7788626@oddjob.uchicago.edu

² High Energy Physics Division, Argonne National Laboratory, Lemont, IL 60439, USA

³ Kavli Institute for Cosmological Physics at the University of Chicago, 5640 South Ellis Avenue, Chicago, IL 60637, USA

⁴ Computer, Computational, and Statistical Sciences Division, Los Alamos National Laboratory, Los Alamos, NM 87545, USA

⁵ Electrical Engineering and Computer Science, Northwestern University, 2145 Sheridan Road, Evanston, IL 60208, USA

However, to fully exploit the burgeoning samples of strong lenses now being reported in various survey datasets (Bolton et al. 2006; Hennawi et al. 2008; Bayliss et al. 2011b; Bayliss 2012; Hezaveh et al. 2013; Stark et al. 2013; Dye et al. 2014) and expected from upcoming surveys (Collett 2015) progress is required on many fronts. For example, currently we are unable to definitely answer even simple questions such as “Is the observed number of giant arcs consistent with theoretical expectations?”. The mismatch between predictions and observations—the so-called “arc-statistics problem”—has remained unresolved for nearly twenty years (Bartelmann et al. 1998; Li et al. 2006; Meneghetti et al. 2013) and deriving clear answers from these new large samples of lenses will require a matched improvement in theoretical predictions and quantification of survey selection effects. Long-standing issues, such as mass sheet degeneracy (Saha 2000; Bradač et al. 2004a; Schneider 2014), also still lurk.

In order to study the above topics systemically, we have developed a pipeline to produce realistic strong-lensed images for cluster- and group-scale lensing systems. PICS is designed to bridge the gap between large-scale surveys for strong lenses, and the largest cosmological N-body simulations now run. The new generation of simulations—and those that will follow—offer, for the first time, both the volume necessary to sample massive halos with good statistics, and the mass resolution to resolve the profiles of typical cluster lenses; both of these features are necessary for robust strong-lensing predictions. The pipeline includes a density estimator based on a resampled Delaunay Tessellation (Schaap & van de Weygaert 2000; Bradač et al. 2004b) technique, a deflection angles calculator based on Fourier methods, a module to build images of sources to be lensed and otherwise included in the light cone, a module for building the images of lens member galaxies, and finally an open-ended module to make the simulated images correspond to observations from a given telescope or survey. PICS can in principle also be used to simulate weak lensing by galaxy clusters, galaxy-galaxy lensing, and substructure lensing near the main cluster or group lenses. The pipeline is optimized to produce large numbers of simulated images—hundred of thousands, or even millions—in reasonable timeframes. This is necessary to match the huge cosmological volumes probed by ongoing and future imaging surveys that cover appreciable fractions of the entire sky.

The statistics of strong lensing are subject to manifold nonlinear effects, many of which are best captured using fully ray-traced N-body or hydro simulations. Examples include effects due to the ellipticity of the lenses (Meneghetti et al. 2003b, 2007), baryonic matter in the lenses (Meneghetti et al. 2003a; Killedar et al. 2012), lens substructure (Hennawi et al. 2007; Meneghetti et al. 2007), structures on the line of sight (Wambsganss et al. 2004; Faure et al. 2009; Bayliss et al. 2014), the mass spectrum normalization (Li et al. 2006; Fedeli et al. 2008, 2010), and the properties of dark matter (Mahdi et al. 2014), in addition to the properties of sources (Keeton 2001b; Wambsganss et al. 2004; Gao et al. 2009). Furthermore, observational effects, of which the simplest is the correlated distribution of image quality, transparency, and sky brightness across multiple filters in a

given survey dataset, will drive the detectability of strong lensing features not just as a function of brightness, but also lensed-image type, arc length-to-width ratio, lensed source color, etc. Consequently, even understanding the selection function of a strong lensing survey, let alone its scientific application, is a challenging task. This challenge is best met by passing realistically simulated images through the same selection process as the real data, which, at least at optical wavelengths, is typically some form of visual selection (e.g., Hennawi et al. 2008; Bayliss et al. 2011b; Wen et al. 2011; More et al. 2012; Stark et al. 2013).

An auxiliary use for this lensing code has been to test the preservation of morphological measurements, such as the Gini coefficient (Abraham et al. 2003), under strong gravitational lensing. In particular, as the new generation of space-based large survey telescopes, e.g., WFIRST⁶, come online, the number of observed strong lensing systems is expected to expand into the thousands. While such systems provide more detailed views of the internal structure of galaxies at higher redshift than would otherwise be possible, the challenge is in extracting useful morphological information from such data. It will likely be necessary to develop morphological measurements that are conserved under gravitational lensing and some elements of the code described here have been used to test the reliability of image plane measurements of the Gini coefficient (Florian et al. 2015a).

The literature is replete with software to simulate cosmological strong lensing, much of which—in order to focus on various physical and computational issues relevant to the calculation—works in a theoretical framework that does not make an explicit link to observations of lenses (e.g., Killedar et al. 2012; Takahashi et al. 2011). Several computational frameworks have been built around cosmologically appropriate distributions of analytic halos, in order to predict strong lensing statistics (Oguri & Blandford 2009; Giocoli et al. 2012). The GLAMER package (Metcalf & Petkova 2014) appears to be the most flexible and general software in the current literature. All such software efforts—including that presented here—must make assumptions and simplifications to enable computational efficiency. Many prior efforts have understandably been forced to use simplified halo models, and single source planes with analytic sources; such simplified systems do not allow generation of simulated observations that appear authentic, and so have in most part avoided attempting to generate such data. The focus of this paper is to establish a strong lensing simulation framework that is aimed at generating large samples of realistic mock observations, primarily of group- and cluster-mass halos. The mass distributions are drawn from extensive N-body simulations, and the source data from the best available Hubble Space Telescope observations, and analyses thereof. The capability for full many-plane lenses and sources is enabled in the code, and significant effort has been expended in order to ‘observe’ the entire light cone simulations, producing image data indistinguishable from real observations.

This paper is structured as follows: In Section 2, we briefly review the basic lensing theory. Details of how to produce lensed images using the data from our cosmolog-

⁶ <http://wfirst.gsfc.nasa.gov>

ical simulations are presented in Section 3. In Section 4, we focus on techniques for making the lensed images realistic in properties and appearance. An illustrative comparison between our results and real observations is shown in Section 5. We discuss the implications and limitations of this image simulation pipeline and conclude in Section 6.

2. BASIC LENSING THEORY

The full formalism described here can be found in Schneider et al. (1992) and Narayan & Bartelmann (1996). Throughout the paper, the thin lens approximation is adopted. The dimensionless surface mass density of a thin lens plane can be written as

$$\kappa(\theta) = \Sigma(\theta)/\Sigma_{\text{crit}}, \quad (1)$$

with the critical surface mass density $\Sigma_{\text{crit}} = (c^2/4\pi G)(D_s)/(D_d D_{ds})$, where D_s and D_d are the angular diameter distances from the source and lens to the observer respectively, D_{ds} is the angular diameter distance from the lens to the source, and $\Sigma(\theta)$ is the surface mass density of the lens. The lensing potential is given by

$$\Psi = \frac{1}{\pi} \int d^2\theta' \kappa(\theta') \ln|\theta - \theta'|. \quad (2)$$

The deflection angles are given by

$$\vec{\alpha}(\vec{\theta}) = \frac{1}{\pi} \int d^2\theta' \kappa(\theta') \frac{\theta - \theta'}{|\theta - \theta'|^2}. \quad (3)$$

Suppose we have obtained the surface mass density on a grid $\kappa_{ij} = \kappa[i, j]$, then the discrete version of Eq. 3 is written as

$$\alpha_{ij} = \frac{1}{\pi} \sum \kappa_{kl} \frac{x_{ij}^{\vec{x}} - x_{kl}^{\vec{x}}}{|x_{ij}^{\vec{x}} - x_{kl}^{\vec{x}}|^2}. \quad (4)$$

If the number of grid cells is large, the direct summation is unacceptably slow. Fourier techniques can be applied to improve the efficiency, because the deflection angle can be written as a convolution of the convergence $\kappa(\vec{\theta})$ with a kernel

$$K = \frac{1}{\pi} \frac{\vec{x}}{|\vec{x}|^2}. \quad (5)$$

This allows the Fourier convolution theorem to be applied, hence

$$\hat{\alpha}(\vec{k}) = \hat{\kappa}(\vec{k}) \hat{K}. \quad (6)$$

Then performing an inverse Fourier transform on the deflection angles in Fourier space, we obtain the deflection angles in real space. The complexity of a Fast Fourier transform (FFT) is only $N \log(N)$, which is much smaller than that of regular summation (N^2), therefore FFT methods speed up the computation of the deflection angle considerably.

Using an FFT to determine the discrete Fourier transform of the convergence $\hat{\kappa}(\vec{k})$ requires the convergence to be periodic on the lens plane, enforced by suitable application of boundary conditions. If the science goal is focused on large scales, periodic boundary conditions are applied. If we want to investigate lensing on small scales,

for example, strong lensing effects around the central regions of galaxy clusters, isolated boundary conditions are applied, following Hockney & Eastwood (1988).

Once the deflection angles at the lens planes are known, we can construct the lensing equation for different source planes. For example, in the case of a single lens plane and a single source plane, the lensing equation can be written as

$$\beta = \theta - \alpha(\theta), \quad (7)$$

where θ is the angular position of the lensed images on the image plane, and β is the angular position of the source images on the source plane. Based on Eq. 7, ray-tracing simulations can be performed from the observer to the lens plane and then to the source plane to produce lensed images. In the case of multiple lens planes, the lensing equation can be written as:

$$\theta^S = \theta - \sum_{i=0}^N \frac{D_{is}}{D_s} \alpha^i(\theta^i), \quad (8)$$

where N is the number of lens planes, D_s is the angular diameter distance from the observer to the source and D_{is} is the angular diameter distance from the i th lens-plane to the source plane. θ^S is the angular position of the source on the source plane, θ is the angular position of the lensed image on the image plane and α^i is the reduced deflection angle on the i th lens-plane. Moreover, if there are also multiple (or many) source-planes, which is typical for a full light cone simulation, one needs to split such a lensing system into sub-systems each with a fully ray-traced single source. These can then be stacked together to produce the full lensed light cone. Further discussion of multiple plane lensing systems can be found in Hilbert et al. (2007) and Petkova et al. (2014). Multiple lens planes and multiple source planes are both enabled within PICS.

3. SIMULATED LENSED IMAGES

Generally, simulations of strongly-lensed arcs include three major steps. First, one requires a mass distribution for the lens or lenses. These may be simple analytic models (Keeton 2001a; Xu et al. 2009), semi-analytic models (Giocoli et al. 2012; McCully et al. 2014) or based on particle distributions from numerical simulations (Dalal et al. 2004; Hilbert et al. 2007; Metcalf & Petkova 2014). PICS is designed to work in the latter regime, with N-body simulations providing mass distributions. As discussed above, one of our principal motivations is arc statistics in large surveys, and simulations naturally capture many of the effects which drive arc counts and properties. With a particle distribution, one also requires a density estimator to calculate the surface mass density map of each lens plane. With a mass map in hand, the next major step is to calculate the deflection field according to the normalized surface density and then build the lensing equation. Finally, ray-tracing is performed to map the locations of pixels in the image plane to the source plane, and—after calculating the flux information of each traced light ray (i.e., by placing images of sources in the source plane)—light rays are mapped from the source plane back onto the lens plane to complete the lensed image. In Figure 1 we provide

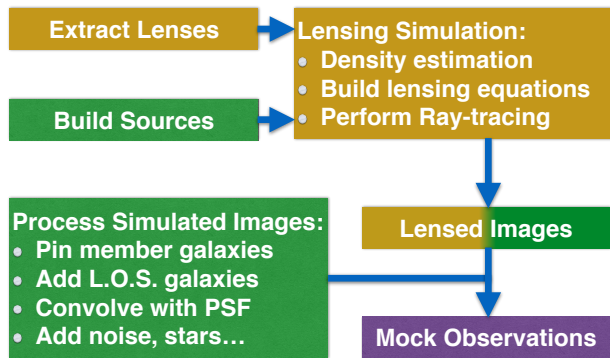


Figure 1. Flowchart of the strong-lensing pipeline - PICS. Yellow denotes simulation results, green, results based on real data, and the purple block is the final output. The simulated lensed images are a combination of real data from HST and the Outer Rim simulation (Cf. Section 3.1). The source light cone used real source images; simulated source images will be added in the future.

a flow chart overview of our PICS pipeline and describe each step in detail below.

3.1. Cosmological Simulations

The cosmological simulation results used in this paper have been obtained with the Hardware/Hybrid Accelerated Cosmology Code (HACC, Habib et al. 2014), a flexible, high-performance N-body code that runs on a range of supercomputing architectures. In this case, we used Mira, a BG/Q system at the Argonne Leadership Computing Facility to carry out the “Outer Rim” simulation, one of the largest cosmological simulations currently available.

The cosmology used is a Λ CDM model close to the best-fit model from WMAP-7 (Komatsu et al. 2011). In detail, the cosmological parameters are: $\omega_{\text{cdm}} = 0.1109$, $\omega_b = 0.02258$, $n_s = 0.963$, $h = 0.71$, and $\sigma_8 = 0.8$. The box size of the simulation is $L = 4225.4 \text{ Mpc} = 3000 h^{-1} \text{ Mpc}$, and it evolves $10,240^3 = 1.07$ trillion particles. This leads to a particle mass of $m_p = 2.6 \cdot 10^9 M_\odot = 1.85 \cdot 10^9 h^{-1} M_\odot$. Extensive testing (Rangel et al. 2015) indicates that at this mass resolution we are able to robustly compute strong lensing for halos of masses $M_{500c} > 2 \cdot 10^{14} h^{-1} M_\odot$ (where $500c$ denotes the overdensity relative to the critical density). (Detailed effects due to substructure in halos, especially at small scales, will be considered later; in this paper our focus is on the strong lensing pipeline itself.)

The large volume ensures that we have high-mass clusters at early times present in the simulation, and extensive statistics for massive systems which individually have large lensing cross sections. For demonstration purposes to illustrate such systems in the latter sections of this paper, we have chosen three massive cluster halos at three different redshifts ($z = 0.736, 0.539, 0.364$) with masses representative of observed South Pole Telescope (SPT) strong lenses (Bleem et al. 2015). Further discussion can be found in Section 5.

Halos are identified with a Friends-of-Friends (FOF) halo finder with a linking length of $b = 0.168$, versus

the canonical value of $b = 0.2$, following Cohn & White (2008) who found that this reduced value mitigates the problem of halo overlinking. Overdensity masses M_{500c} of the clusters in the simulation are computed based on the centers of the FOF halos. These centers are determined by finding the potential minimum for each cluster.

We have identified the subhalos in each cluster using a phase-space based subhalo finder. There are a number of ways to identify substructure in halos; two commonly used ways are running a hierarchical FOF algorithm (as used in, e.g., Rockstar, Behroozi et al. 2013) or using a local overdensity finder (as used in, e.g., SUBFIND, Springel et al. 2001). Such approaches can be enhanced by also using velocity information to determine if a particle actually belongs to a subhalo or is a member of the main halo (e.g., the subfinding algorithm in Rockstar). Our approach is based on local density estimation and folds in phase-space information as well. We first organize all particles that were found by the FOF halo finder into a Barnes-Hut tree structure (Barnes & Hut 1986) to provide them in an easily accessible format. A smooth particle hydrodynamics (SPH) kernel is then used to estimate the local density for each particle (very similar to the original SUBFIND approach). Particles are assigned into subhalo candidates and we build an initial membership list for the main halo as well as subhalo candidates. The final step is to determine if a particle is bound to a subhalo or in fact belongs to the main halo. Here we calculate the total energy for each particle (kinetic plus potential) to determine its escape velocity with regard to the subhalo. We investigate each particle one by one, testing if it belongs to the subhalo, and if it does not, we assign it to the main halo. If a particle gets removed from the subhalo, a new energy calculation is carried out and the remaining particles are investigated. This procedure continues iteratively until only bound particles remain in the subhalo candidate. Finally, we set a minimum number of particles for a subhalo to be considered viable (20 particles in this case) and subhalo candidates with fewer particles than this limit are discarded. Each final subhalo catalog provides positions, orientations, ellipticities and masses, and this data is used in combination with data from real observations to “paint” cluster member galaxies onto simulated images (Section 4).

3.2. Density Estimator

Our algorithm for computing the surface density from a halo particle set implements the Delaunay tessellation field estimator (DTFE) method proposed by Schaap and Weygaert (Schaap & van de Weygaert 2000). The DTFE method requires the Delaunay triangulation⁷ of the halo particles to obtain the local gradients of the 3D density function. This first order interpolation method assumes the gradient within a tetrahedron to be constant and discontinuous at its boundaries. The field value for an arbitrary point, \vec{x} , is interpolated using the Delaunay vertices $\vec{x}_0, \vec{x}_1, \vec{x}_2, \vec{x}_3$ of the containing tetrahedron by

$$\widehat{f}(\vec{x}) = f(\vec{x}_0) + \widehat{\nabla} f|_{\text{Del}} \cdot (\vec{x} - \vec{x}_0), \quad (9)$$

⁷ A Delaunay triangulation of a discrete 3D point set P is a triangulation $DT(P)$ such that the circumscribing sphere of a tetrahedron contains no other points in P .

where $\widehat{\nabla f}|_{Del}$ is the estimated constant field gradient using the known field values $f(\vec{x}_0), f(\vec{x}_1), f(\vec{x}_2), f(\vec{x}_3)$. For density field reconstruction, the on-site density values are estimated by the inverse volume of the contiguous Voronoi cell, thereby ensuring mass conservation. The estimated density for each input, \vec{x}_i , is given by

$$\widehat{\rho(\vec{x}_i)} = \frac{(d+1)m}{\sum_{j=1}^{N_{\mathcal{T},i}} V(\mathcal{T}_{j,i})}, \quad (10)$$

where $N_{\mathcal{T},i}$ denotes the number of tetrahedra $\mathcal{T}_{j,i}$ having \vec{x}_i as a vertex, m is the mass, and $(d+1)$ is the tetrahedral volume normalization factor.

We compute the surface density field as a 2D uniform grid, where each grid cell represents the average surface density of vertical paths filling a $\Delta x \times \Delta y \times \ell$ vertical column in the 3D density field. From the equation for surface density along a vertical path, given by

$$\Sigma(\vec{\xi}) = \int \rho(\vec{\xi}, z) dz, \quad (11)$$

where z is the vertical coordinate, and $\vec{\xi}$ is a 2D field point, it follows that the surface density value for a grid cell covering the region S is given by

$$\bar{\Sigma}_S = \frac{\int_{\Delta y} \int_{\Delta x} \Sigma(\vec{\xi}) d\xi_1 d\xi_2}{\int_{\Delta y} \int_{\Delta x} d\xi_1 d\xi_2}, \quad \vec{\xi} \in S. \quad (12)$$

In our algorithm, we calculate the optimal DTFE value for Eq. 11 by

$$\widehat{\Sigma(\vec{\xi})} = \sum_{i=1}^{N_{\mathcal{T},\vec{\xi}}} \rho(\vec{\xi}, \widehat{mid}(\mathcal{T}_{i,\vec{\xi}}, \vec{\xi})) \text{len}(\mathcal{T}_{i,\vec{\xi}}, \vec{\xi}), \quad (13)$$

where $N_{\mathcal{T},\vec{\xi}}$ denotes the number of tetrahedra $\mathcal{T}_{i,\vec{\xi}}$ intersecting the vertical path of $\vec{\xi}$, \widehat{mid} is a function for determining the midpoint of a line-tetrahedron intersection, and len is a function for determining the length of the intersection. We use the optimal DTFE surface density in a Monte Carlo (MC) approximation for Eq. 12, where the number of MC samples is weighted by the number density of input particles in the 3D vertical column.

3.3. Making A Catalog of Source Images

Source galaxies are selected from the Hubble Ultra Deep Field (Beckwith et al. 2006, HUDF). The HUDF data offer high spatial resolution relative to the resolution of the ground-based telescopes that our image simulations are intended to imitate and are sufficiently deep that they sample the high-redshift galaxies which form the bulk of the strongly-lensed population. A drawback of the dataset is that the sampled area is relatively small, and so cosmic variance is a possible concern. This is discussed further in Section 6 below.

In the simulated images shown below, we have limited our analysis to three HUDF bands: F435W, F505W, and F775W. Individual galaxies in the HUDF were selected by first stacking the images in these three bands, and then cutting at a threshold of 2.0σ above the background noise level and keeping only pixels that had at least three

neighboring pixels that were also at or above the threshold. Any pixels that were removed by this initial cut, but that were surrounded on all sides by pixels that were not removed and that all belonged to the same object were also kept. The final set of pixels for each source, which we refer to as an *aperture mask*, then defines ‘live’ pixels which must be considered when ray-tracing a particular source. The complete list of potential sources was then refined to include only those that match objects in the photometric redshift catalog of Coe et al. (2006). That analysis is a detailed look at the HUDF data, including redder bands not considered here, and is more than sufficiently deep to sample even the faintest sources relevant for simulating ground-based survey imaging.

Once an aperture mask is made for all viable source galaxies, subfields of the HUDF are chosen to become part of the light cone for gravitational lensing in the ray-tracing code. The width of these subfields was chosen to be about four times larger than the largest caustic structures in the simulation, resulting in subfields of 1000×1000 pixels. The centers of subfields are chosen randomly, but with the requirement that the entire 1000×1000 pixel region contains data from the HUDF (i.e., does not extend past the edges of the field).

The redshift of each galaxy in a given subfield is taken to be the maximum-likelihood value from the photometric redshift catalogue of Coe et al. (2006). To streamline computation, source galaxies are binned by redshift. Because the effects of gravitational lensing (e.g., the size of the Einstein radius) vary most rapidly at redshifts that also happen to have the highest galaxy counts, the bins were selected using a simple calculation such that each bin has an equal number of galaxies (except for the highest redshift bin, which was allowed to have fewer galaxies than the others). This allows for narrow redshift bins when lensing effects are rapidly changing, but also minimizes the number of redshifts for which deflection angle maps were required. A complete ray-trace is then performed for the median redshift of each bin, rather than for each source. All galaxies in each redshift bin are treated as if they were at that bin’s median redshift.

3.4. Performing Ray-tracing Simulations

With the surface mass density of the lens or lenses in hand, as well as a set of source planes, the next step is to compute the deflection angle field at each lens plane. To do this, we first build a grid at each lens plane. Because we use Fourier methods to boost the efficiency of the convolution (see Eq. 4), we use a regular mesh⁸. For each lens plane on the grid we then compute the deflection angle field at each position.

When light rays cross the lens plane, they are deflected with an angle

$$\tilde{\alpha} = \frac{4G}{c^2} \int d^2\xi' \Sigma(\vec{\xi}') \frac{\vec{\xi} - \vec{\xi}'}{|\vec{\xi} - \vec{\xi}'|^2}, \quad (14)$$

where $\Sigma(\xi)$ is the surface mass density on the lens plane,

⁸ The use of adaptive meshes is also an alternative option for increasing computational speed. However, with a static grid and Fourier methods, we prefer to simply decrease the pixel size on the lens plane to make higher quality simulated images if and as necessary, since computational cost is not a limiting factor compared to the resources necessary to make the input simulations.

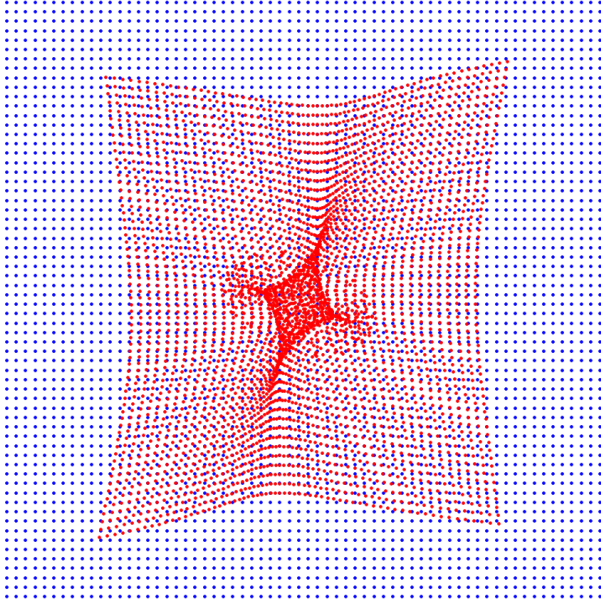


Figure 2. Illustration of mapping the lens plane to the source plane. Blue points show the positions of the intersection between light rays which start from the observer, and the image plane. To produce the lensed images using Fourier methods, we sample the blue points on regular grids. Red points illustrate the intersection between the deflected light rays and the source plane.

ξ is the physical position on the lens plane, and $\tilde{\alpha}$ is the physical deflection angle—i.e., it is the angle between the extension line of incoming light rays and the outgoing light rays at the lens plane. The relation between the physical deflection angle $\tilde{\alpha}(\xi)$ and the reduced deflection angle $\alpha(\theta)$ is written as

$$\alpha(\theta) = \frac{D_{\text{ds}}}{D_s} \tilde{\alpha}(D_d \theta) . \quad (15)$$

The deflected light rays travel to the source plane, and intersect with the source plane. For the single image plane and single source plane case, we can use Eq. 7 to find the source plane positions directly. For multiple lens plane and multiple source plane cases, the physical deflection angle is calculated first, and we then use the relation in Eq. 15 to scale the physical deflection angles to reduced deflection angles, and the positions in the source plane can be determined by using Eq. 8. We are now ready to ray-trace and make lensed images on the image plane⁹.

On the image plane, the pipeline default output pixel size and scale for output ray-traced images is 0.09 arcsec/pixel, and 2048×2048 pixels. This output sampling is sensibly coarser than the input source plane sampling, coarse enough to provide a reasonable field of view with 2048×2048 pixels (just beyond 3×3 arcminutes, sufficient for even very massive lenses) while still providing a much finer sampling than the typical ground-based telescope point spread function.

With the image plane established, the second step is to use the deflection angle fields established above to

⁹ Note that in a system with a single lens plane, the “image” plane and the “lens” plane coincide. This is not generally true; the image plane is coincident with only the lowest redshift lens plane in more complex systems.

trace light rays from the image plane to the source plane. Figure 2 shows an illustration of tracing light rays from the observer through the image plane to the source plane in the simple case of a single lens plane. We assume that the grid points (blue points) are the intersections of the image plane and the light rays which start from the observer.

With the lensing geometry now fully described for each pixel of the image plane, the final step is to propagate brightness information from the source plane back to the image plane. The brightness of each ray is computed from the source plane brightness information as described by the cataloged HUDF source images. Since the rays intersecting the source plane sample the pixelated source plane irregularly, interpolation is applied. Three interpolation schemes have been considered: linear interpolation, bicubic interpolation and bicubic-spline interpolation. We conclude that the improvement from either bicubic and bicubic-spline interpolation is limited, and—as we are focused on arc statistics from ground-based imaging data—not worth the extra computational time. Linear interpolation is thus the default method. After calculating the brightness for each traced light ray, that data is mapped back to the image plane. Following Figure 2, we now have the brightness at each red point, the one-to-one relationship between the blue points and red points, and hence we obtain the brightness at the blue points, which is simply the pixelated image of the image plane. For the typical case of multiple source planes, sampling the redshift distribution of sources, this entire process is iterated across the redshift bins and the resulting image sub-planes stacked to produce the final result. An example simulated lensed image is shown in Figure 3. In this simulated lensing system, an input light cone of sources is picked from the HUDF as described above with an area of 30 × 30 arcseconds. The surface mass density of the lens plane is calculated by applying our improved density estimator to a cluster-sized halo from the Outer Rim simulation. The M_{500c} of this halo is $4.8 \times 10^{14} M_\odot$, and its redshift is 0.539. For clarity, in Figure 3 we show only the central 81 × 81 arcseconds or 900 × 900 pixels at a sampling of 0.09 arcsec/pixel; the computed image from which this is drawn is 2048 × 2048 pixels, as described above.

4. ADDING THE LIGHTCONE AND CLUSTER GALAXIES

The previous sections describe in detail how the image simulation pipeline produces only strongly lensed images. To make simulated images that appear realistic, we must further add several other image components and simulate observation by a telescope and camera system. Elements of this portion of the overall simulation pipeline include

- galaxies belonging to the lens itself (which, in the case of a massive and/or low-redshift cluster lens and shallow observations, can dominate the image),
- other galaxies along the line of sight which are not significantly lensed (because they are either in front of the lens plane, or behind it but at large impact angles) and
- faint stars.

The final image stack is then passed through an open-ended module which “observes” the field; basically this

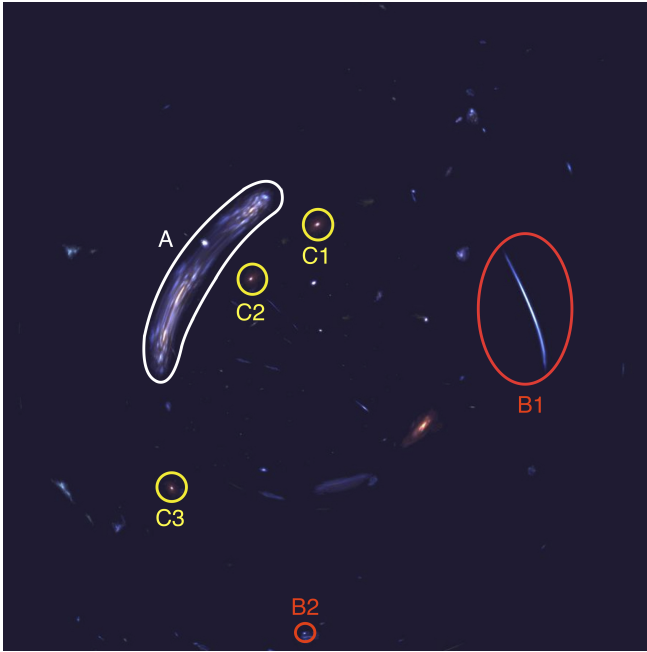


Figure 3. An example simulated lensed image with 900×900 pixels at a sampling of 0.09 arcsec/pixel. The lensing is due to an $M_{500} = 4.5 \times 10^{14} M_{\odot}$ halo at $z=0.539$. The white aperture (A) marks a lensed giant arc, with the source in this case located near a naked caustic cusp; the red apertures (B) mark a merging pair image forming a giant lensed arc and a third image of the same source, with the source of these images located around a fold caustic; the yellow circles (C) mark three lensed images, of which the source is located near the same naked caustic cusp as the source in image A.

process entails: convolution with a telescope point spread function (PSF) model, re-binning to the final desired sampling, and adding noise elements that replicate the real data being mimicked (including elements such as chip defects and cosmic rays, if required). Bright stars, which typically show telescope- and camera-specific oddities such as chip bleeding, are added at this final stage and treated separately, as discussed in below in Section 4.4.

4.1. Lens Member Galaxies

The principal focus of our work is lensing by galaxy clusters and groups, and what follows is appropriate to “painting” galaxies on to dark matter halos of that mass scale. While the strong lensing pipeline can in principle be used to describe lenses of arbitrary masses, at single-galaxy mass scales inputs other than large scale cosmological N-body simulations would be appropriate for generating the strong lensing signals, and we do not attempt to model such systems here.

As it is our intention to use PICS to model and analyse extensive survey data, the fundamental methodology we have in mind is to draw photometric information about cluster and group member galaxies from such survey data. However, such a treatment is left for future papers, as it will be perforce a survey- and data-specific task. To make progress here, and demonstrate the utility of PICS, we instead draw photometric information from the Second Red-Sequence Cluster Survey (Gilbank et al. 2011, RCS2) as inputs into simulated cluster-scale lensing images. Specifically, we use the background corrected photometry of several massive clusters in the RCS2 at

$0.5 < z < 0.6$, the richness of which indicate masses comparable to galaxy clusters in the South Pole Telescope Survey cluster sample of Bleem et al. (2015), as the fiducial values for cluster member magnitudes in the *griz* bands (the native observed bands in the RCS2 data). The cluster member photometry is corrected, to first order, for measurement scatter in the fainter galaxies by moving galaxies toward the red-sequence colors that dominate cluster members in cluster cores. We do this by keeping the *r*-band magnitudes fixed and perturbing both the *g*- and *i*-bands toward the red sequence colors (i.e., redder galaxies become bluer, bluer galaxies conversely become redder). Individual magnitudes are changed by a one-sided Gaussian random draw from the measured magnitude errors, hence with the presumption made that most galaxies in truth have colors closer to the red sequence, and have scattered away from it in the input RCS2 catalog due to measurement uncertainties. We also clean the input photometric catalogs of objects with extreme colors—these are overwhelmingly faint objects that are poorly measured to be extremely red or blue in $g-r$, $r-i$, or $i-z$. Section 5 demonstrates simulated images of strong lensing from $0.3 < z < 0.8$. For clusters at redshifts different than the input photometry, a simple band-dependent shift in magnitudes is applied to make the magnitudes and colors of galaxies on the red-sequence correct for the simulated redshift. These are derived with *k*-corrections based on an elliptical galaxy spectrum in the same cosmology as the Outer Rim simulation. Bluer cluster members will not be exactly correct, but for demonstration purposes this is sufficient.

The photometric catalog is then matched to the subhalo catalog drawn from the N-body simulation, with assignments made at random. Typically, the list of observed cluster members is longer than the list of subhalos, since the input cluster photometry probes to masses smaller than the subhalo catalog; the subhalo list is padded to the appropriate length using a random draw of particle positions from the main halo.

An algorithm that matches the cluster member photometry to the subhalos by rank ordering, with the most luminous galaxy assigned to the most massive subhalo, and so on, will suffer from bias due to the dynamical erosion of subhalo masses as they are accreted into cluster cores, an effect which will preferentially decrease the mass-to-light ratio of cluster members near the cluster center. In the future, we will use subhalo mass and photometry matching via subhalo-finding algorithms that track subhalos temporally through the entire multi-petabyte outputs of the Outer Rim simulation, allowing the spatially dense luminous component to be assigned to dark matter subhalos based on their masses upon accretion into the larger system, before significant mass-loss occurs. Note also that the brightest cluster galaxy is assigned to the center (potential minimum) of the main halo.

Before simulating images of cluster galaxies, we must further specify the sizes, shapes, luminosity profiles and orientations of the cluster galaxies. The orientations and ellipticities are taken from the subhalo catalog. Those galaxies assigned to random halo points are given an arbitrary orientation; ellipticities are drawn at random from a distribution shaped to approximate the distribution of projected axis ratios for elliptical galaxies as found by

Ryden (1992).

The radial light profiles of all galaxies are described by Sérsic profiles—a Sérsic index of 1 for pure disks, and ranging from 3 to 8 for the bulge component—as well as a bulge-to-total ratio (B/T) for each galaxy. All galaxies with colors in $r - z$ redder than 0.2 magnitudes bluer than the red-sequence are assigned a bulge-to-total ratio in z -band of $B/T_z = 1$. Galaxies with $r - z$ bluer than $r - z = 0$, effectively the blue edge of the cluster galaxy distribution, are assigned a bulge-to-total ratio in the z -band of $B/T_z = 0.1$. Galaxies in between these two limits are assigned z -band bulge-to-total ratios linearly interpolated between 0.1 to 1, according to their $r - z$ color. The bulge-to-total ratios in the bluer filters are then assigned as a power of the z -band value: for example the most different is the bluest filter, $B/T_g = B/T_z^{1.25}$. This ensures that bluer galaxies observed in the bluer bands are more ‘disky’ than in the redder bands, while the pure bulge—i.e., elliptical—galaxies are such in all four filters. The bulge component of galaxies for galaxies fainter than $M_z^* + 1$ are assigned a Sérsic index of 3, and the brightest cluster galaxy is assigned a Sérsic index of 8, with values interpolated between these limits according to the z -band magnitude, consistent with the distribution observed in low redshift galaxy cluster members (Fasano et al. 2012).

The sizes of the bulge component of cluster member galaxies with flux F are assigned simply as $C + 1/2 \log F$, with the constant C chosen such that the effective radius of the largest galaxies is ~ 8 kpc, consistent, for example, with that seen for the local giant elliptical M87 (Murphy et al. 2011). Disk sizes, similarly, are assigned using a linear relationship between galaxy area and luminosity to replicate the disk size distribution seen in Laurikainen et al. (2010). The brightest cluster member is allowed to vary up to one magnitude brighter or fainter than the RCS2 fiducial, and is described by a two component Sérsic model where one component has a size $5\times$ that of the other, approximately simulating the extended stellar halo often seen around central galaxies. The luminosity fraction assigned to this component is allowed to vary from 25-75% of the total galaxy light.

The details of the size and light profile assignments sketched above are admittedly ad hoc. However in simulating optical images of intermediate redshift cluster galaxies, observed from the ground, they are sufficient. Actually measuring the morphology of such galaxies requires Hubble Space Telescope observations (Dressler et al. 1997) and so in truth the exact details—at the level of the fundamental plane for example (Kormendy et al. 2009, e.g.)—matter little in creating images that look realistic in this context. Additionally, we remind the reader that the intended use of this image simulation pipeline is primarily to create large sets of simulated images matched to large sets of actual survey data, from which the distributions of properties of the lens galaxies would be directly drawn; the simulation approach sketched above serves only to allow illustration of the pipeline absent this close coupling to a particular survey dataset.

With a list of observable properties in-hand (the sources of which are summarized in Table 1) the actual images of lens member galaxies are made using the open-source `GalSim` package (Rowe et al. 2014), an astro-

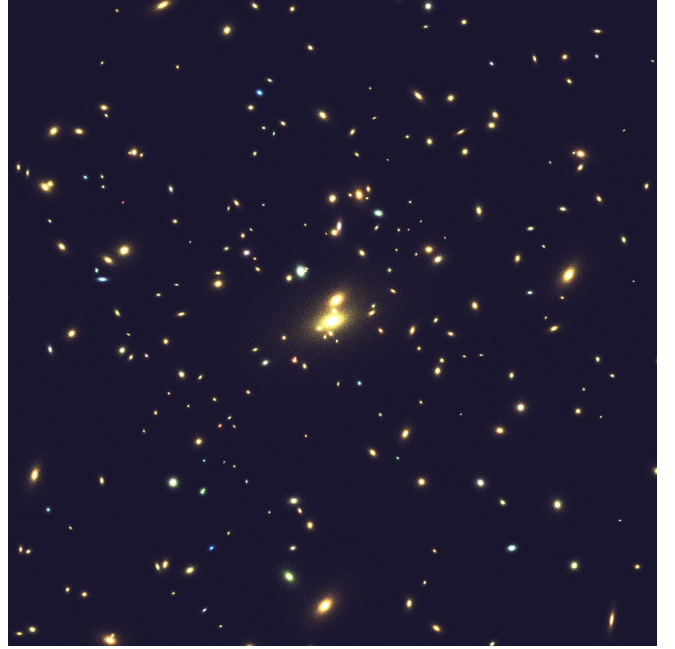


Figure 4. An example of simulated member galaxies of a cluster lens. The size of this field is approximately $3' \times 3'$, i.e. with 2048^2 pixels at an angular size per pixel of $0''.09$.

nomical image simulation toolkit designed primarily to enable characterization of weak-lensing estimators with accuracy sufficient to meet the requirements of future Stage IV Dark Energy surveys. Here we simply use the mock galaxy generation routines to create images of the member galaxies following the parameterizations sketched above. We use the photon shooting method, in which the surface brightness profile of the galaxies are finitely sampled, and generate a high-resolution, low-noise¹⁰ fits image of the cluster in each of our desired filter bands. An example of the output from the `GalSim` routine is shown in Figure 4.

Property	Source
Position	Outer Rim Simulation
Orientation	Outer Rim Simulation
Axis Ratio	Outer Rim Simulation
Multi-filter magnitudes	RCS2 Data
Bulge to disk ratio (per filter)	ad hoc
Bulge half light radius	Fit to Literature
Disk scale radius	Fit to literature
Sersic index	Literature

Table 1
Properties of Lens Member Galaxies and Provenance.

4.2. Adding Galaxies on the Line of Sight

Galaxies on the line of sight that are not strongly lensed are another important component of realistic strong lensing images. One method to add these is to build a full light cone with galaxies on the line of sight, and then ray-trace as above through the whole light cone. The advantage of this method is that the lensed images

¹⁰ The Poisson noise inherent in the photon-shooting step is subdominant to the observational noise added below.

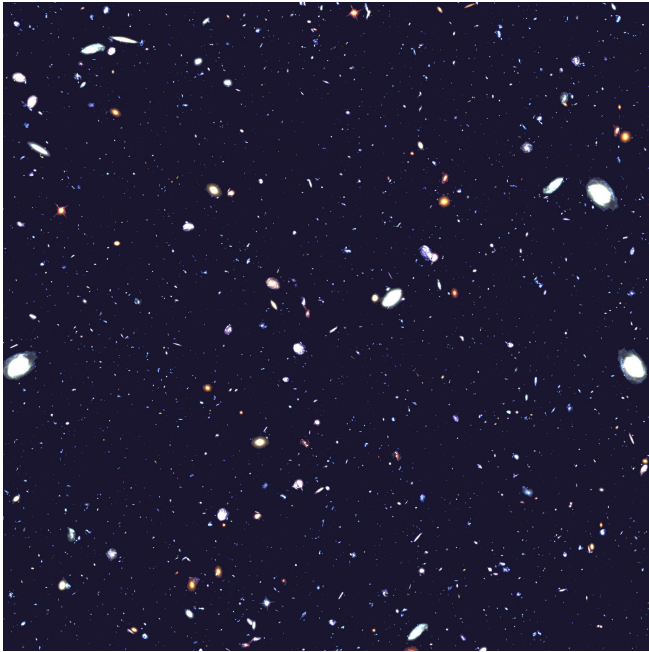


Figure 5. Example of simulated images of galaxies on the line of sight. The size of the field of view and the resolution are the same as the Figure 4.

that result reflect all parts of the lensing signal (i.e., both strong and weak lensing) and that the results are accurate, especially in the weak-lensing regime, where such techniques are widely applied (Jain et al. 2000; Vale & White 2003; Hilbert et al. 2009; Killedar et al. 2012). The disadvantage of this method is its computational cost.

The other method, and the one used here, is to fully ray-trace only a small light cone which covers the caustics of the lenses, where strong lensing happens. This provides images of any galaxies that are significantly magnified, but drops weak lensing signals far from the center of the lens. The next step is to build a light cone image without ray-tracing, and finally to stack both together. The advantage of this method is its computational efficiency; this is especially important for studies of strong lensing effects since—as strong lensing is a rare phenomenon—many instances must be run. This is the basic method adopted here.

To build an image of the unlensed light cone, we consider the galaxies within the HUDF, as described in Section 3.4. Performing random sampling with replacement, we obtain a sample of galaxies for a given field of view. The galaxy number density of the produced image is the same as HUDF, and the image is originally built at the native sampling of the processed HUDF images of $0''.03$ per pixel. Galaxies are pinned to the image at random positions and orientations—i.e., no correlation functions are built into the distribution. Finally, the complete image of the entire field of view is rebinned to the requested pixelization (typically $0''.09$ per pixel for images discussed here), taking care to ensure conservation of total flux. A sample image of simulated galaxies along the line of sight is shown in Figure 5.

4.3. Stacking the Image Components

Stacking the image of lensed galaxies, the image of galaxies on the line of sight, and the image of member

galaxies produces the final realistic lensed image containing all the important extra-galactic components. Care must be taken here to ensure the appropriate scaling of each sub-image, in each filter. The HUDF data, for example, is not in the identical filters as the RCS2 images from which the cluster member photometry is derived, and the photometric zeropoints of each subimage are not necessarily identical. Moreover, neither are likely perfectly matched to the filter set of the real survey images for which matching simulated images are being constructed. In the current realisation of the pipeline, this aspect of the final image construction is handled simplistically, since the image sub-sets used are similar enough that simple bulk scalings, applied at the image level, are sufficient to harmonize all the image subsets before summing them. We proceed simply by adjusting all input image zeropoints to that of the output simulated image in each desired filter, adjusting for both overall sensitivity, and filter shifts.

Filter differences—for example with the HUDF F435W filter as input, being mapped into a desired g-band output image—are accounted for by applying a bulk scaling to the entire image that is based on the typical color ($g - F435W$) for galaxies in the HUDF field of view. In principle, when shifting the HUDF data into other even nearby bandpasses, one should account for the spectrum and redshift of each galaxy individually, as modest shifts in bandpass may have quite large effects on flux if, for example, one is sampling Lyman-break galaxies. However, it is worth noting that the typical lensed galaxy is at $z \sim 2$ (Bayliss 2012), for which the above simple (and fast) technique is likely sufficient.

Note also that the time-saving strategy employed in the ray-tracing means that the central portion of the stacked image is actually over-populated with distant (i.e., more distant than the lens) galaxies. These galaxies are generally very faint—most too faint to appear in any significant number in typical ground-based imaging. There is no discernible over-density in a single image even when not degraded to ground-based seeing and depth—see Figure 6. However, one cannot measure the expected de-magnification depletion behind massive lenses using these images; for such a measure, or weak lensing measurements in general, a larger field ray-trace must be adopted.

4.4. Adding Bright Stars

Bright stars are added to the simulated image in two steps. The majority of stars—i.e., those which can be described as a point source convolved with a model PSF—are drawn from an analysis of the image set to be simulated. In practice, in a large set of survey data, this information would be drawn from photometric catalogs that span the many images of the survey. Note that proper star-galaxy separation, which can be a significant issue in ground based data, is not worrisome in this context; at the depths where this becomes problematic, galaxy counts wholly dominate over star counts at high galactic latitudes. From a visual perspective, ensuring the inclusion of stars that are obviously point sources, and hence bright enough to be robustly isolated in analysis of ground-based images, is sufficient. For the example images detailed in Section 5 below, the majority of bright stars have been added as single pixel point sources to the

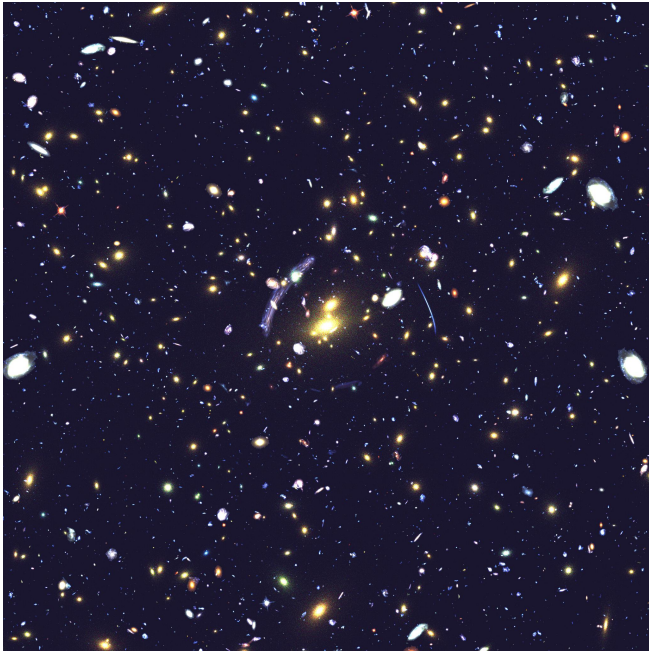


Figure 6. Example simulated image with all components added except bright stars. The size of the field of view and the resolution are the same as the Figure 4. This image is effectively a stack of Figures 3, 4, and 5.

stacked image above, using data drawn from a catalog of stars constructed by measuring unresolved sources in the real image these examples are designed to replicate.

For the brightest stars—i.e., those for which the PSF becomes visibly complex due to optical effects such as scattered light and ghosting, and/or detector effects such as charge bleeding—the pipeline uses a different strategy. Such stars are added *after* the stacked image is convolved with a nominal telescope PSF (see Section 4.5 below) by drawing on a catalog of image examples taken from the real imaging data that the pipeline is simulating. Image cutouts of bright stars are grafted in the simulated images using a ragged boundary that is undetectable in the final image product. This boundary is essentially defined algorithmically as a noisy version of a low level isophote constructed by thresholding the star image on a stack of all input images (typically three, if one is simulating a suite of color images). Several examples of this can be seen in Figure 7.

4.5. Convolution with a PSF and Rebinning

The entire image stack is next convolved with a PSF model. A simple Moffat function (Moffat 1969) is used as the model. The normalized Moffat profile is a two-parameter function of the form

$$I(r) = \left[1 + \left(\frac{r}{\alpha} \right)^2 \right]^{-\beta}, \quad (16)$$

where α to first order describes the core of the PSF and β the wings, and the oft-used full-width-at-half-maximum (FWHM) value of such a profile is given by

$$\text{FWHM} = 2\alpha\sqrt{2^{1/\beta} - 1}. \quad (17)$$

One of the necessary elements of simulating data realistically is to allow for both the variation and correlation in

PSFs both within an image location between filters, and across a dataset of multiple locations. We achieve this in the most straightforward manner possible, by measuring the Moffat parameters for each image in a dataset, and then drawing sets of PSF descriptions (a set being all three filters, in the case of a typical color image) from the same location in the survey data, but otherwise at random. Once convolved with the appropriate PSF, each image is also re-binned, conserving flux, to the final desired pixel scale, which is set by the imaging data being simulated.

Care must be taken in the PSF convolution to use a large enough convolution kernel such that the brightest image elements—generally, point sources—do not show any significant edge effects from the convolution box, once appropriate image noise is added (see below). This is determined experimentally for any simulated image set. It is desirable to keep the convolution box small for rapidity of calculation; how one balances this against the typical PSF and noise properties of a particular dataset to be simulated is best determined at run time.

4.6. Adding Noise

The final step in producing the simulated images is to add noise. In PICS, the amount and character of noise added to each image is guided by the noise statistics of the real data being simulated. The baseline noise added is simply Poisson noise, with amplitudes set by the real data. Like in the PSF convolution, this is done by drawing a set of noise levels jointly across all filters under consideration, to ensure the strong correlations that often exist between filters in an imaging survey are sampled (in particular if that imaging survey is taken in a mode where all filters are imaged near-simultaneously at a given sky location). The default algorithm actually selects both the PSF values and the sky noise levels from the same location in the real imaging survey, as there may also be correlations between sky levels and PSFs in real data.

Beyond simple Poisson noise, the pipeline also adds other noise elements, which are crafted to match the specifics of the particular data being simulated. Examples can be seen in the images in Section 5 below, and are discussed in detail there.

5. RESULTS

The SPT cluster sample (Bleem et al. 2015) contains dozens of newly discovered strong lenses. The optical imaging follow-up data used in Bleem et al. is heterogeneous by optical imaging survey standards, as it is a collection of pointed follow-up observations taken with a variety of telescopes used in a wide range of observing conditions. These real data thus serve as an excellent point of comparison for further demonstrating the image simulation pipeline described in detail above.

We have chosen for this purpose three example strong lensing SPT clusters that are not representative of the typical SPT followup data but rather illustrate the range of such data, and also span the cluster redshift range where the bulk of cluster strong lensing signals are expected for massive clusters (Hennawi et al. 2008). The details of these three clusters, and the optical observations of them, are given in Table 2. In brief, the lowest redshift system, SPT-CL J2325-4111 (ACO S1121 Abell

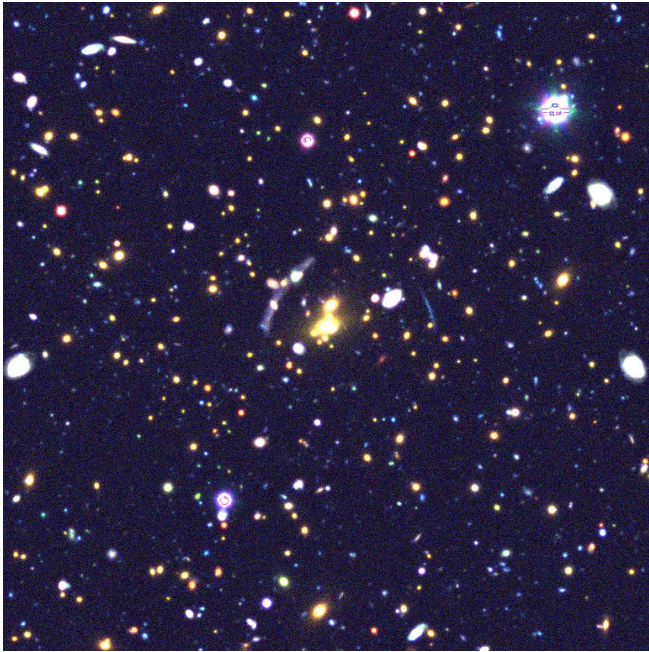


Figure 7. Example of a final simulated image after “observing”—i.e., convolution with an appropriate PSF, rebinning, and addition of noise and bright stars. This image completes the pipeline sequence illustrated in Figures 2-6.

et al. (1989)), is a particularly massive and optically-rich cluster, and the data used here are from the CTIO 4 m telescope¹¹ and MOSAIC-II camera. These data are modestly deep but were taken under conditions of extremely poor seeing.

SPT-CL J0307-5042, at a moderate redshift, illustrates a strong-lensing system with several strongly-lensed sources, and excellent data, i.e., long integrations with the MegaCam imager (McLeod et al. 2015) at the 6.5 m Magellan II Clay telescope¹², taken with seeing well less than one arcsecond. The highest redshift system, SPT-CL J0142-5032, is a cluster strong lens showing a single bright giant arc, imaged quite shallowly using the 1 m Swope telescope¹³. This combination of shallow imaging, a small telescope, and a higher redshift cluster renders all but the brightest cluster members near-invisible, and is illustrative of a cluster detected at the sensitivity limit of a ground-based wide-field imaging survey. Each of these real clusters also illustrates some potential limitations of our methodology; these are discussed further in Section 6. The simulated halos chosen to approximate these real SPT strong lenses are each within 0.02 in redshift of the real systems, and differ by less than 10% from the measured mass (i.e., well within the photometric redshift and mass uncertainties). All three are taken from the Outer Rim simulation described in Section 3.1.

Figures 8 and 9 illustrate the shallowest images, from the Swope 1 m telescope. In each case we leave it here as an exercise for the reader to determine which of the two images is the real cluster, and which the simulation using the pipeline tuned to match such data. An answer

key is provided in Section 6. Figures 10 and Figures 11 illustrate data from the CTIO 4 m telescope. Finally, Figures 12 and Figures 13 illustrate data from the 6.5 m Magellan telescopes.

Figures 10-13 demonstrate noise window-paning due to observations with a mosaic camera, which results in cross-hatched stripes of enhanced noise at inter-chip gaps, or even small regions with no data. Figures 8-11 demonstrate two forms of chip defects and cosmic rays. In Figures 8-9 these defects are compact, but the real image has been processed using SWarp (Bertin et al. 2002) to shift to a final output. This results in a slight ringing in the image around sharp features. This effect is captured in the image simulation by first creating a set of template blank images with cosmic rays using IRAF’s *mknoise* function, tuned to match the statistics of the cosmic rays seen in the real data, and then sampling and interpolating sub-images from that template set in order to make instances of cosmic rays that include the subtler images features induced by the processing of the real data. Figures 10-11 conversely show how the pipeline adds more complex cosmic ray tracks. In this case the real data being matched shows a small number of cosmic ray tracks that traverse many pixels and appear ‘worm-like’. The same basic algorithm that was used to add the brightest star images to the simulated images is used in this case; actual images of these cosmic rays are extracted from the real data, and added to the simulations.

6. DISCUSSION

PICS produces simulated images of strong lensing for halos over a wide range in mass. We have focused our attention in this first paper on demonstrating the efficacy of this pipeline for the most massive strong lenses—i.e., massive clusters such as the recent sample from the SPT (Bleem et al. 2015). Searches for strong lensing in imaging data—at least at optical wavelengths—have often proceeded by visual searches (e.g., Gladders et al. 2003; Hennawi et al. 2008; Bayliss et al. 2011b; Wen et al. 2011; More et al. 2012; Stark et al. 2013; Marshall et al. 2015) as the human eye offers remarkable sensitivity to complex patterned signals in the low signal-to-noise regime. The aim of PICS is thus to produce rigorous strong-lensing calculations, by ray-tracing extensive N-body simulations, and to couple these calculations to a suite of algorithms capable of simulating the entire light cone of an observation. These light cones can then be ‘observed’ to produce realistic simulated images which are essentially indistinguishable from real telescope data even to the expert eye. Figures 8-13 give three paired examples of the outcomes: Figures 9,10,13 are real SPT strong lenses, and Figures 8,11,12 the matched simulated images.

A further goal is to enable the production of such images in large numbers with a reasonable computational burden; exactly what constitutes ‘reasonable’ in this context is framed by the computational cost of the input simulations, and the surveys and imaging data to which such simulations are compared. Regardless, it is instructive to consider the computational cost for a single image, such as shown in Figures 8-13. PICS images can be produced on workstations or on parallel supercomputers. Timing examples of these two use cases are:

¹¹ <http://www.ctio.noao.edu/noao/content/victor-blanco-4-m-telescope>

¹² <https://obs.carnegiescience.edu/Magellan>

¹³ <https://obs.carnegiescience.edu/swope>

Cluster Name	Redshift	$M_{500} h_{70}^{-1} M_{\odot}$	Telescope & Camera (Pixel Scale)	Filters	Seeing(FWHM in ")
SPT-CL J2325-4111	0.36	7.55×10^{14}	CTIO 4m+MOSAIC II (0".3)	g, r, i	2.10,1.95,1.89
SPT-CL J0307-5042	0.55	5.26×10^{14}	Magellan 6.5m+MegaCam (0".16)	g, r, i	0.90,0.47,0.73
SPT-CL J0142-5032	0.73	5.75×10^{14}	Swope 1m+SITe3 (0".50)	V, R, I	1.30,1.16,1.14

Table 2
Properties of the Clusters and Imaging Data, from Bleem et al. (2015).

- a test based on producing a single image, from a pipeline instance executing on a single thread on one core of a data analysis workstation, a.k.a. ‘DataStar’. This computer, used for local and real-time data analysis tasks, provides 24 dual-threaded Xeon E5-2620 cores running at 2.0 GHz, with ample memory resources.
- a test based on producing 1000 images, one from each of 1000 pipeline instances, running in parallel on a total of 1000 cores on the NERSC supercomputer ‘Edison’. Edison is a Cray XC30 supercomputer with 133,824 cores, where each core is an Intel ‘Ivy Bridge’ 2.4Ghz processor, again with ample memory resources. Edison represents a highly parallelized compute environment, suitable for considering resources for large production runs of this image simulation pipeline.

The lens density estimation takes a little less than half the time, roughly equal time is spent on ray-tracing, generating member galaxy images, and galaxy images along the line of sight. The computational cost of the deflection angle field and ‘observing’ the image stack is sub-dominant.

Note that the calculations directly related to the strong lensing take about 60% of the total time, and that at this pace one could produce about 20,000 simulated images on a workstation scale computer like DataStar in a week of runtime. The individual calculations on the Edison are slower, however, a one week run using only a modest 4% of the available power of that machine would produce ~ 1 million simulated strong lensing images, such as one might carry out as an input to the analysis of a survey covering a large fraction of the entire sky.

The primary purpose of these simulated images is to enable the study of arc statistics, by providing a robust link between real data and simulation predictions. A second paper in this series will explore this application in detail for the SPT cluster sample. However, it is worth noting that the pipeline itself is sufficiently flexible to enable a number of other studies. Elements of this pipeline have been used to study lensing effects on the morphologies of background source galaxies (Florian et al. 2015a, in prep) and the utility of the Gini coefficient as a constraint when identifying image families in strong lensing systems (Florian et al. 2015b, in prep). In the longer term, development of automated strong-lens-finding algorithms (e.g., Seidel & Bartelmann 2007; Marshall et al. 2009; Joseph et al. 2014; Gavazzi et al. 2014) will be enhanced by the ready availability of large libraries of realistic test images against which algorithmic advances may be rigorously tested. Moreover, only minor tweaks to the pipeline as laid out here, or changes to the background source, will enable full simulation of weak lensing in galaxy clusters, including lensing of the cosmic mi-

crowave background by clusters. Changes to the input mass field, in order to better accommodate the effects of baryonic structures in individual galaxies, will also enable studies of galaxy-galaxy lensing.

PICS has, however, some limitations which must be considered in the context of some applications or real datasets. Several issues arise due to the use of the HUDF as the input data for ray-tracing source planes. The first issue is the angular area—and cosmological volume—covered by these data. For the brightest galaxies at any redshift, the HUDF does not provide well-sampled statistics with negligible cosmic variance. Thus, it fails to include the occasional bright low- z galaxy which does appear in real data along lines of sight to known strong lenses: see, for example, the bright, resolved late-type galaxy adjacent to the strong lens in Figure 9. This same limitation also makes the statistics of only the very brightest arcs—those that come from systems with highly magnified and intrinsically bright galaxies (e.g., Wuyts et al. 2012)—questionable when using only the HUDF as a source input. Moreover, if one is simulating a field larger than the HUDF, repetition of individual galaxies in the unlensed light-cone outputs is unavoidable, and can produce visual hints that the image in question is simulated: see, for example, the three instances of the same recognizable spiral galaxy that appear on the left and right edges of the light cone example images in Figure 5. All three of these related issues can (and will) be addressed in a future iteration of this pipeline by both grafting wider-field multi-band HST observations (which, perforce, will be shallower) together with the HUDF and by sampling the source planes with a ‘wedding-cake’ strategy that minimizes the effects of the HUDF’s small field of view while still exploiting its depth, image quality, and extensive characterization in the literature.

However, even the HUDF, or the yet deeper refined dataset the HST eXtreme Deep Field (Illingworth et al. 2013), fail fundamentally to address one limitation of using real images as inputs to strong-lensing ray-tracing: namely that the strongly-lensed images provide access to smaller spatial scales in the source plane due to magnification. This limitation is insignificant when simulating most ground-based data, but at spatial resolutions of $\sim 0.5''$ or better, such as when comparing the best ground-based imaging to equivalent simulations (see Figure 13 compared to Figure 12), the lack of finer spatial detail in the HST-based input data starts to become apparent. This effect will be obvious when simulating high-resolution space-based observations of strong lensing. To address this requires the generation of spatial information in the source plane at scales finer than the best available data. In some applications, redshifting images of low redshift galaxies to high redshift provides the necessary inputs (e.g., Florian et al. 2015a). However, for large-

scale survey predictions, a more robust method that adds spatial complexity to deep extant HST images is likely needed. One approach may be to use rapid galaxy-image-simulation tools such as GAMER (Groeneboom & Dahle 2014) to complexify HST images.

Multiple lens-planes are also enabled in the image simulation pipeline. For large sample arcs statistics, some claim that the effects of structure on the line of sight is modest ($\lesssim 7\%$, Hennawi et al. 2007), though Puchwein & Hilbert (2009) assert a boost of $10\% - 25\%$ if the effects of additional structures along the line of sight are included, and Wambsganss et al. (2005) note that the magnitude of the boost is a strong function of source redshift. Doubtless, for high accuracy lensing modeling (Inoue & Takahashi 2012; D’Aloisio et al. 2014) and time delay measurements of a single lensing system, the lensing effects of the structure on the line of sight should be taken into account (McCully et al. 2014; Bayliss et al. 2014), and simulations of gravitational lensing with multiple planes are needed. We will investigate the influence of structures on the line of sight on gravitational lensing systematically in a future paper, using the multiple lens-plane capabilities of the code presented here.

In this work, a gravity-only N-body simulation is used, in part because the primary aim of this paper is to describe the image simulation pipeline, rather than to discuss in detail issues of resolution, N-body versus hydrodynamical simulations, galaxy modeling in clusters, etc when computing strong lensing statistics, issues to which we will return in future work. The effects of baryonic matter on the cross section of cluster-scale strong lensing will need to be considered. Observationally, Newman et al. (2013) show that the total density profile of the central galaxy and the dark matter halo in massive clusters can be described by an NFW profile (Navarro et al. 1996), implying that the presence of baryonic matter does not significantly change the original form of the density profile in massive cluster-scale halos. Regarding substructure, as shown by Nagai & Kravtsov (2005) using hydrodynamical simulations, baryons do affect the subhalos at scales smaller than the virial radius ($\lesssim 0.2r_{vir}$) but not significantly at larger radii. Lensing effects due to baryonic matter in the member galaxies cannot ultimately be ignored, because gravitationally lensed arcs which are produced by member galaxies are observed (Halkola et al. 2006; Sand et al. 2008; Newman et al. 2009). Regardless, the presence or lack of disagreement between simulations and observations of strong lensing remains an open question and we anticipate that the simulation toolkit described here will add usefully to that ongoing discussion.

This research was funded in part by the Strategic Collaborative Initiative administered by the University of Chicago’s Office of the Vice President for Research and for National Laboratories. Argonne National Laboratory’s work was supported under the U.S. Department of Energy contract DE-AC02-06CH11357. This research used resources of the ALCF, which is supported by DOE/SC under contract DE-AC02-06CH11357 and resources of the OLCF, which is supported by DOE/SC under contract DE-AC05-00OR22725. Some of the results presented here result from awards of computer time

provided by the ASCR Leadership Computing Challenge (ALCC) programs at Argonne and Oak Ridge (ALCF and OLCF). This work was also supported in part by the Kavli Institute for Cosmological Physics at the University of Chicago through grant NSF PHY-1125897 and an endowment from the Kavli Foundation and its founder Fred Kavli. We also thank the South Pole Telescope collaboration for allowing the usage of the SPT cluster follow-up imaging shown in this work.

REFERENCES

- Abell, G. O., Corwin, Jr., H. G., & Olowin, R. P. 1989, *ApJS*, 70, 1
- Abraham, R. G., van den Bergh, S., & Nair, P. 2003, *ApJ*, 588, 218
- Barnes, J., & Hut, P. 1986, *Nature*, 324, 446
- Bartelmann, M., Huss, A., Colberg, J. M., Jenkins, A., & Pearce, F. R. 1998, *A&A*, 330, 1
- Bayliss, M. B. 2012, *ApJ*, 744, 156
- Bayliss, M. B., Gladders, M. D., Oguri, M., et al. 2011a, *ApJ*, 727, L26
- Bayliss, M. B., Hennawi, J. F., Gladders, M. D., et al. 2011b, *ApJS*, 193, 8
- Bayliss, M. B., Johnson, T., Gladders, M. D., Sharon, K., & Oguri, M. 2014, *ApJ*, 783, 41
- Beckwith, S. V. W., Stiavelli, M., Koekemoer, A. M., et al. 2006, *AJ*, 132, 1729
- Behroozi, P. S., Wechsler, R. H., & Wu, H.-Y. 2013, *ApJ*, 762, 109
- Bertin, E., Mellier, Y., Radovich, M., et al. 2002, in *Astronomical Society of the Pacific Conference Series*, Vol. 281, *Astronomical Data Analysis Software and Systems XI*, ed. D. A. Bohlender, D. Durand, & T. H. Handley, 228
- Bhattacharya, S., Habib, S., Heitmann, K., & Vikhlinin, A. 2013, *ApJ*, 766, 32
- Bleem, L. E., Stalder, B., de Haan, T., et al. 2015, *ApJS*, 216, 27
- Bolton, A. S., Burles, S., Koopmans, L. V. E. and Treu, T., & Moustakas, L. A. 2006, *ApJ*, 638, 703
- Bradač, M., Lombardi, M., & Schneider, P. 2004a, *A&A*, 424, 13
- Bradač, M., Schneider, P., Lombardi, M., et al. 2004b, *A&A*, 423, 797
- Coe, D., Benítez, N., Sánchez, S. F., et al. 2006, *AJ*, 132, 926
- Coe, D., Zitrin, A., Carrasco, M., et al. 2013, *ApJ*, 762, 32
- Cohn, J. D., & White, M. 2008, *MNRAS*, 385, 2025
- Collett, T. E. 2015, *ApJ*, 811, 20
- Dalal, N., Holder, G., & Hennawi, J. F. 2004, *ApJ*, 609, 50
- D’Aloisio, A., Natarajan, P., & Shapiro, P. R. 2014, *MNRAS*, 445, 3581
- Dressler, A., Oemler, Jr., A., Couch, W. J., et al. 1997, *ApJ*, 490, 577
- Dye, S., Negrello, M., Hopwood, R., et al. 2014, *MNRAS*, 440, 2013
- Fasano, G., Vanzella, E., Dressler, A., et al. 2012, *MNRAS*, 420, 926
- Faure, C., Kneib, J.-P., Hilbert, S., et al. 2009, *ApJ*, 695, 1233
- Fedeli, C., Bartelmann, M., Meneghetti, M., & Moscardini, L. 2007, *A&A*, 473, 715
- . 2008, *A&A*, 486, 35
- Fedeli, C., Meneghetti, M., Gottlöber, S., & Yepes, G. 2010, *A&A*, 519, A91
- Gao, G. J., Jing, Y. P., Mao, S., Li, G. L., & Kong, X. 2009, *ApJ*, 707, 472
- Gavazzi, R., Marshall, P. J., Treu, T., & Sonnenfeld, A. 2014, *ApJ*, 785, 144
- Gilbank, D. G., Gladders, M. D., Yee, H. K. C., & Hsieh, B. C. 2011, *AJ*, 141, 94
- Giocoli, C., Meneghetti, M., Bartelmann, M., Moscardini, L., & Boldrin, M. 2012, *MNRAS*, 421, 3343
- Gladders, M. D., Hoekstra, H., Yee, H. K. C., Hall, P. B., & Barrientos, L. F. 2003, *ApJ*, 593, 48
- Gould, A., & Yee, J. C. 2014, *ApJ*, 784, 64
- Grillo, C., Suyu, S. H., Rosati, P., et al. 2015, *ApJ*, 800, 38
- Groeneboom, N. E., & Dahle, H. 2014, *ApJ*, 783, 138
- Habib, S., Pope, A., Finkel, H., et al. 2014, *ArXiv e-prints*, arXiv:1410.2805

- Halkola, A., Seitz, S., & Pannella, M. 2006, *MNRAS*, 372, 1425
- Han, C., Jung, Y. K., Udalski, A., et al. 2013, *ApJ*, 778, 38
- Han, J., Eke, V. R., Frenk, C. S., et al. 2015, *MNRAS*, 446, 1356
- Hennawi, J. F., Dalal, N., Bode, P., & Ostriker, J. P. 2007, *ApJ*, 654, 714
- Hennawi, J. F., Gladders, M. D., Oguri, M., et al. 2008, *AJ*, 135, 664
- Hezaveh, Y. D., Marrone, D. P., Fassnacht, C. D., et al. 2013, *ApJ*, 767, 132
- Hilbert, S., Hartlap, J., White, S. D. M., & Schneider, P. 2009, *A&A*, 499, 31
- Hilbert, S., White, S. D. M., Hartlap, J., & Schneider, P. 2007, *MNRAS*, 382, 121
- Hockney, R. W., & Eastwood, J. W. 1988, *Computer simulation using particles*
- Hoekstra, H., & Jain, B. 2008, *Annual Review of Nuclear and Particle Science*, 58, 99
- Illingworth, G. D., Magee, D., Oesch, P. A., et al. 2013, *ApJS*, 209, 6
- Inoue, K. T., & Takahashi, R. 2012, *MNRAS*, 426, 2978
- Jain, B., Seljak, U., & White, S. 2000, *ApJ*, 530, 547
- Jones, T. A., Ellis, R. S., Schenker, M. A., & Stark, D. P. 2013, *ApJ*, 779, 52
- Jones, T. A., Swinbank, A. M., Ellis, R. S., Richard, J., & Stark, D. P. 2010, *MNRAS*, 404, 1247
- Joseph, R., Courbin, F., Metcalf, R. B., et al. 2014, *A&A*, 566, A63
- Keeton, C. R. 2001a, *ArXiv Astrophysics e-prints*, astro-ph/0102341
- . 2001b, *ApJ*, 562, 160
- Kelly, P. L., Rodney, S. A., Treu, T., et al. 2014, *The Astronomer's Telegram*, 6729, 1
- Kilbinger, M., Fu, L., Heymans, C., et al. 2013, *MNRAS*, 430, 2200
- Killedar, M., Lasky, P. D., Lewis, G. F., & Fluke, C. J. 2012, *MNRAS*, 420, 155
- Kneib, J.-P., & Natarajan, P. 2011, *A&A Rev.*, 19, 47
- Komatsu, E., Smith, K. M., Dunkley, J., et al. 2011, *ApJS*, 192, 18
- Kormendy, J., Fisher, D. B., Cornell, M. E., & Bender, R. 2009, *ApJS*, 182, 216
- Laurikainen, E., Salo, H., Buta, R., Knapen, J. H., & Comerón, S. 2010, *MNRAS*, 405, 1089
- Li, G. L., Mao, S., Jing, Y. P., et al. 2006, *MNRAS*, 372, L73
- Liao, K., Treu, T., Marshall, P., et al. 2015, *ApJ*, 800, 11
- Limousin, M., Ebeling, H., Ma, C.-J., et al. 2010, *MNRAS*, 405, 777
- Limousin, M., Ebeling, H., Richard, J., et al. 2012, *A&A*, 544, A71
- Mahdi, H. S., van Beek, M., Elahi, P. J., et al. 2014, *MNRAS*, 441, 1954
- Mandelbaum, R., Seljak, U., Kauffmann, G., Hirata, C. M., & Brinkmann, J. 2006, *MNRAS*, 368, 715
- Mandelbaum, R., Slosar, A., Baldauf, T., et al. 2013, *MNRAS*, 432, 1544
- Mao, S. 2012, *Research in Astronomy and Astrophysics*, 12, 947
- Marshall, P. J., Hogg, D. W., Moustakas, L. A., et al. 2009, *ApJ*, 694, 924
- Marshall, P. J., Verma, A., More, A., et al. 2015, *ArXiv e-prints*, arXiv:1504.06148
- Massey, R., Kitching, T., & Richard, J. 2010, *Reports on Progress in Physics*, 73, 086901
- Massey, R., Rhodes, J., Leauthaud, A., et al. 2007, *ApJS*, 172, 239
- McCully, C., Keeton, C. R., Wong, K. C., & Zabludoff, A. I. 2014, *MNRAS*, 443, 3631
- McLeod, B., Geary, J., Conroy, M., et al. 2015, *PASP*, 127, 366
- Meneghetti, M., Argazzi, R., Pace, F., et al. 2007, *A&A*, 461, 25
- Meneghetti, M., Bartelmann, M., Dahle, H., & Limousin, M. 2013, *Space Sci. Rev.*, 177, 31
- Meneghetti, M., Bartelmann, M., & Moscardini, L. 2003a, *MNRAS*, 346, 67
- . 2003b, *MNRAS*, 340, 105
- Meneghetti, M., Rasia, E., Vega, J., et al. 2014, *ApJ*, 797, 34
- Metcalf, R. B., & Petkova, M. 2014, *MNRAS*, 445, 1942
- Moffat, A. F. J. 1969, *A&A*, 3, 455
- More, A., Cabanac, R., More, S., et al. 2012, *ApJ*, 749, 38
- Muraki, Y., Han, C., Bennett, D. P., et al. 2011, *ApJ*, 741, 22
- Murphy, J. D., Gebhardt, K., & Adams, J. J. 2011, *ApJ*, 729, 129
- Nagai, D., & Kravtsov, A. V. 2005, *ApJ*, 618, 557
- Narayan, R., & Bartelmann, M. 1996, *ArXiv Astrophysics e-prints*, astro-ph/9606001
- Navarro, J. F., Frenk, C. S., & White, S. D. M. 1996, *ApJ*, 462, 563
- Newman, A. B., Treu, T., Ellis, R. S., & Sand, D. J. 2011, *ApJ*, 728, L39
- . 2013, *ApJ*, 765, 25
- Newman, A. B., Treu, T., Ellis, R. S., et al. 2009, *ApJ*, 706, 1078
- Oguri, M., Bayliss, M. B., Dahle, H., et al. 2012, *MNRAS*, 420, 3213
- Oguri, M., & Blandford, R. D. 2009, *MNRAS*, 392, 930
- Okabe, N., Takada, M., Umetsu, K., Futamase, T., & Smith, G. P. 2010, *PASJ*, 62, 811
- Paraficz, D., & Hjorth, J. 2010, *ApJ*, 712, 1378
- Peter, A. H. G., Rocha, M., Bullock, J. S., & Kaplinghat, M. 2013, *MNRAS*, 430, 105
- Petkova, M., Metcalf, R. B., & Giocoli, C. 2014, *MNRAS*, 445, 1954
- Puchwein, E., & Hilbert, S. 2009, *MNRAS*, 398, 1298
- Richard, J., Stark, D. P., Ellis, R. S., et al. 2008, *ApJ*, 685, 705
- Rowe, B., Jarvis, M., Mandelbaum, R., et al. 2014, *ArXiv e-prints*, arXiv:1407.7676
- Rozo, E., Nagai, D., Keeton, C., & Kravtsov, A. 2008, *ApJ*, 687, 22
- Ryden, B. 1992, *ApJ*, 396, 445
- Saha, P. 2000, *AJ*, 120, 1654
- Sand, D. J., Treu, T., Ellis, R. S., Smith, G. P., & Kneib, J.-P. 2008, *ApJ*, 674, 711
- Schaap, W. E., & van de Weygaert, R. 2000, *A&A*, 363, L29
- Schneider, P. 2014, *A&A*, 568, L2
- Schneider, P., Ehlers, J., & Falco, E. E. 1992, *Gravitational Lenses*, ed. Schneider, P., Ehlers, J., & Falco, E. E.
- Seidel, G., & Bartelmann, M. 2007, *A&A*, 472, 341
- Sereno, M., & Covone, G. 2013, *MNRAS*, 434, 878
- Springel, V., White, S. D. M., Tormen, G., & Kauffmann, G. 2001, *MNRAS*, 328, 726
- Stark, D. P., Auger, M., Belokurov, V., et al. 2013, *MNRAS*, 436, 1040
- Stark, D. P., Richard, J., Charlot, S., et al. 2014, *ArXiv e-prints*, arXiv:1408.3649
- Suyu, S. H., Marshall, P. J., Auger, M. W., et al. 2010, *ApJ*, 711, 201
- Suyu, S. H., Auger, M. W., Hilbert, S., et al. 2013, *ApJ*, 766, 70
- Suyu, S. H., Treu, T., Hilbert, S., et al. 2014, *ApJ*, 788, L35
- Takahashi, R., Oguri, M., Sato, M., & Hamana, T. 2011, *ApJ*, 742, 15
- Treu, T. 2010, *ARA&A*, 48, 87
- Treu, T., Marshall, P. J., Cyr-Racine, F.-Y., et al. 2013, *ArXiv e-prints*, arXiv:1306.1272
- Umetsu, K., & Broadhurst, T. 2008, *ApJ*, 684, 177
- Vale, C., & White, M. 2003, *ApJ*, 592, 699
- van Engelen, A., Keisler, R., Zahn, O., et al. 2012, *ApJ*, 756, 142
- Wambsganss, J., Bode, P., & Ostriker, J. P. 2004, *ApJ*, 606, L93
- . 2005, *ApJ*, 635, L1
- Wen, Z.-L., Han, J.-L., & Jiang, Y.-Y. 2011, *Research in Astronomy and Astrophysics*, 11, 1185
- Wuyts, E., Rigby, J. R., Gladders, M. D., et al. 2012, *ApJ*, 745, 86
- Xu, D. D., Mao, S., Wang, J., et al. 2009, *MNRAS*, 398, 1235

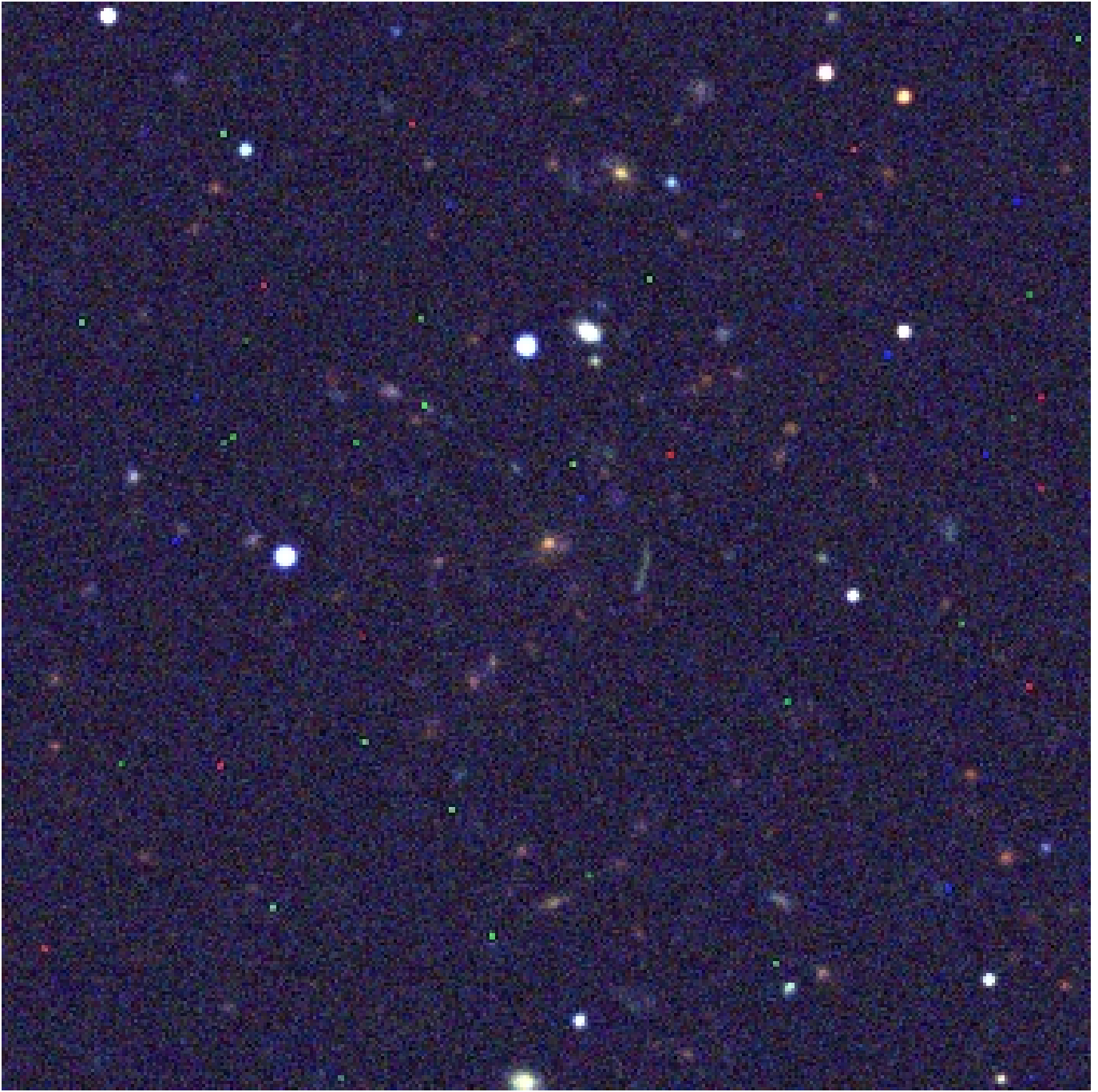


Figure 8. Example Swope 1 m observed strong lens from the SPT cluster sample, either a simulated or real image. An answer key is provided in Section 6.

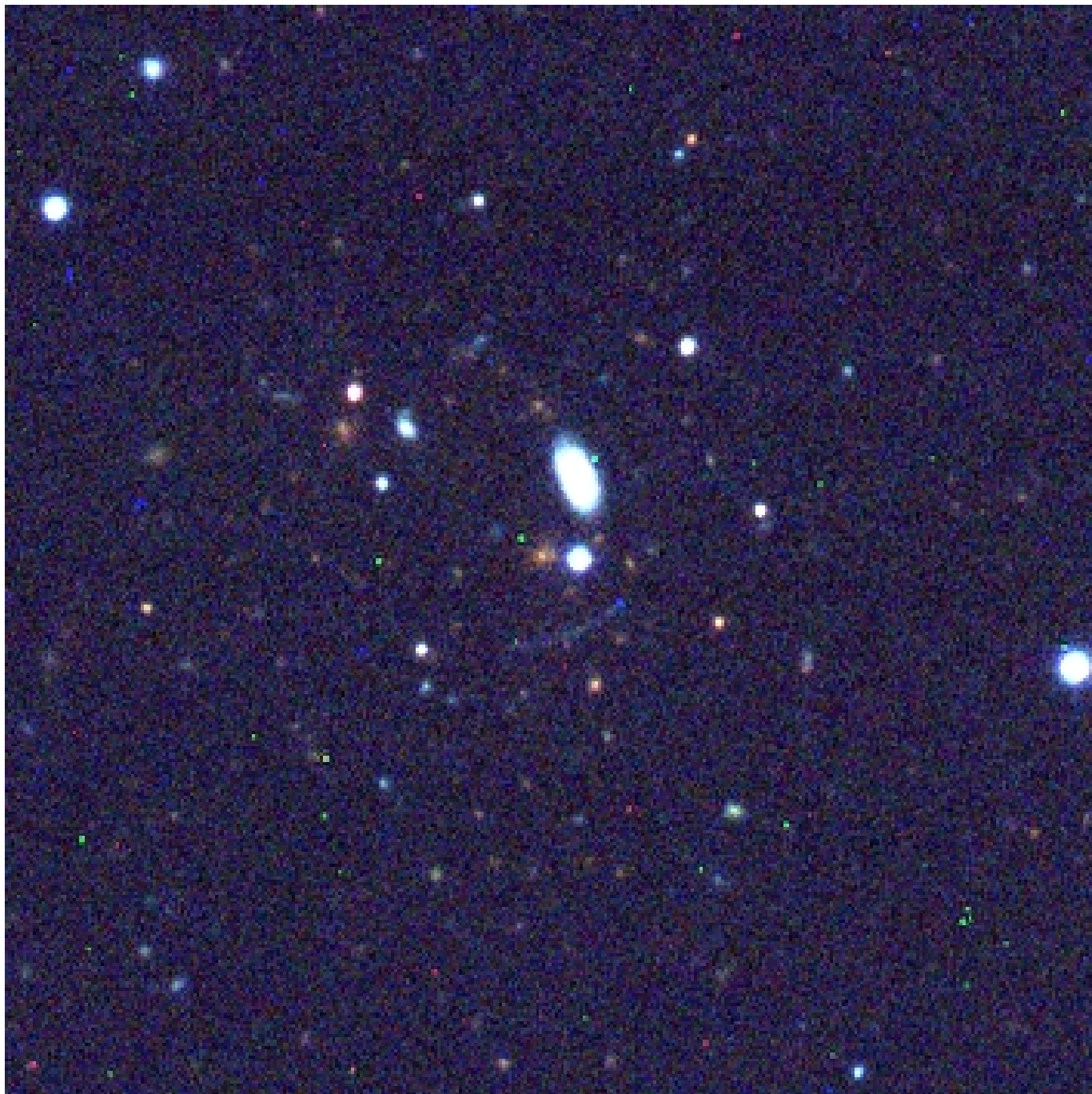


Figure 9. Example Swope 1 m observed strong lens from the SPT cluster sample, either a simulated or real image.

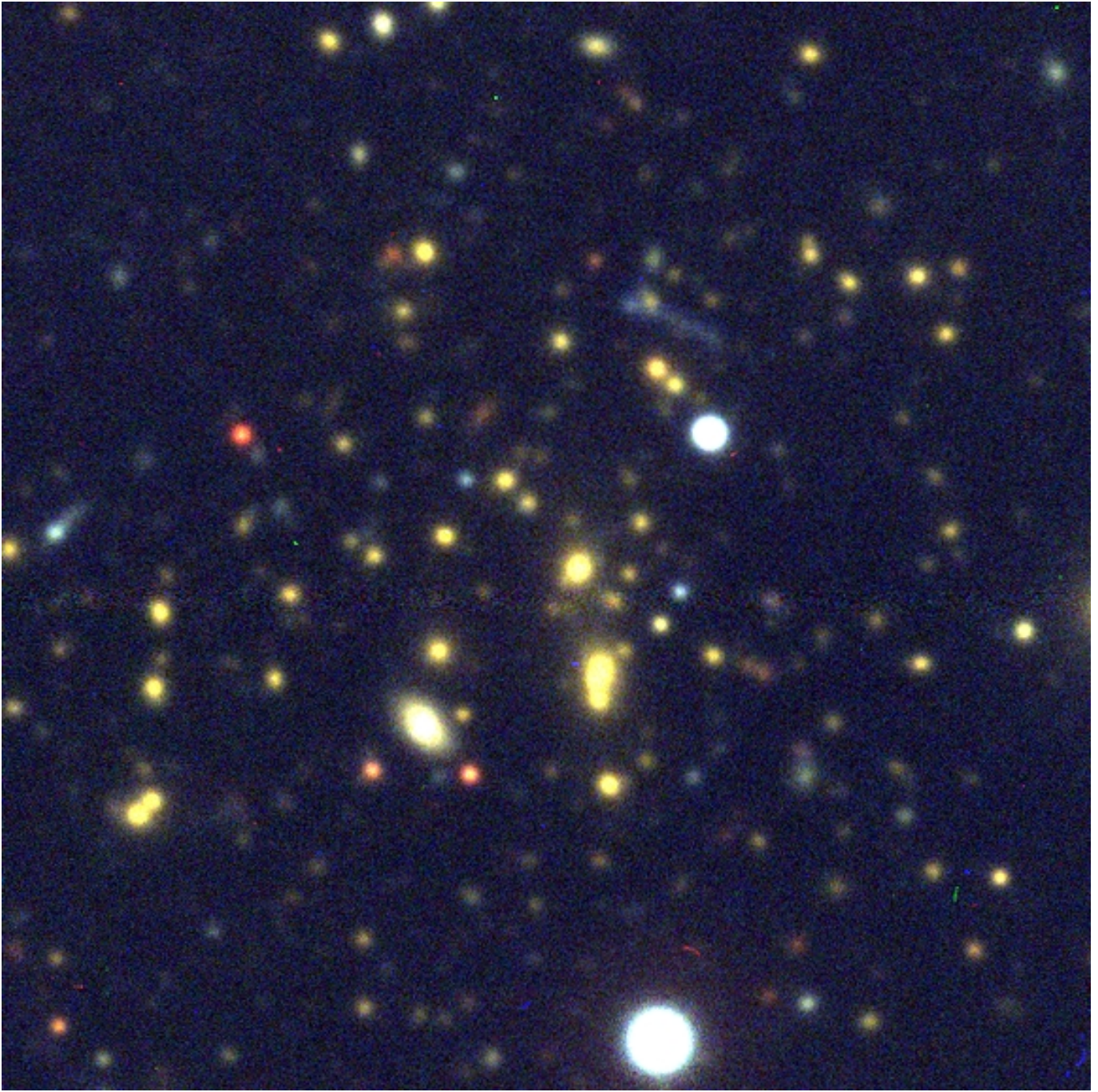


Figure 10. Example CTIO 4 m observed strong lens from the SPT cluster sample, either a simulated or real image.

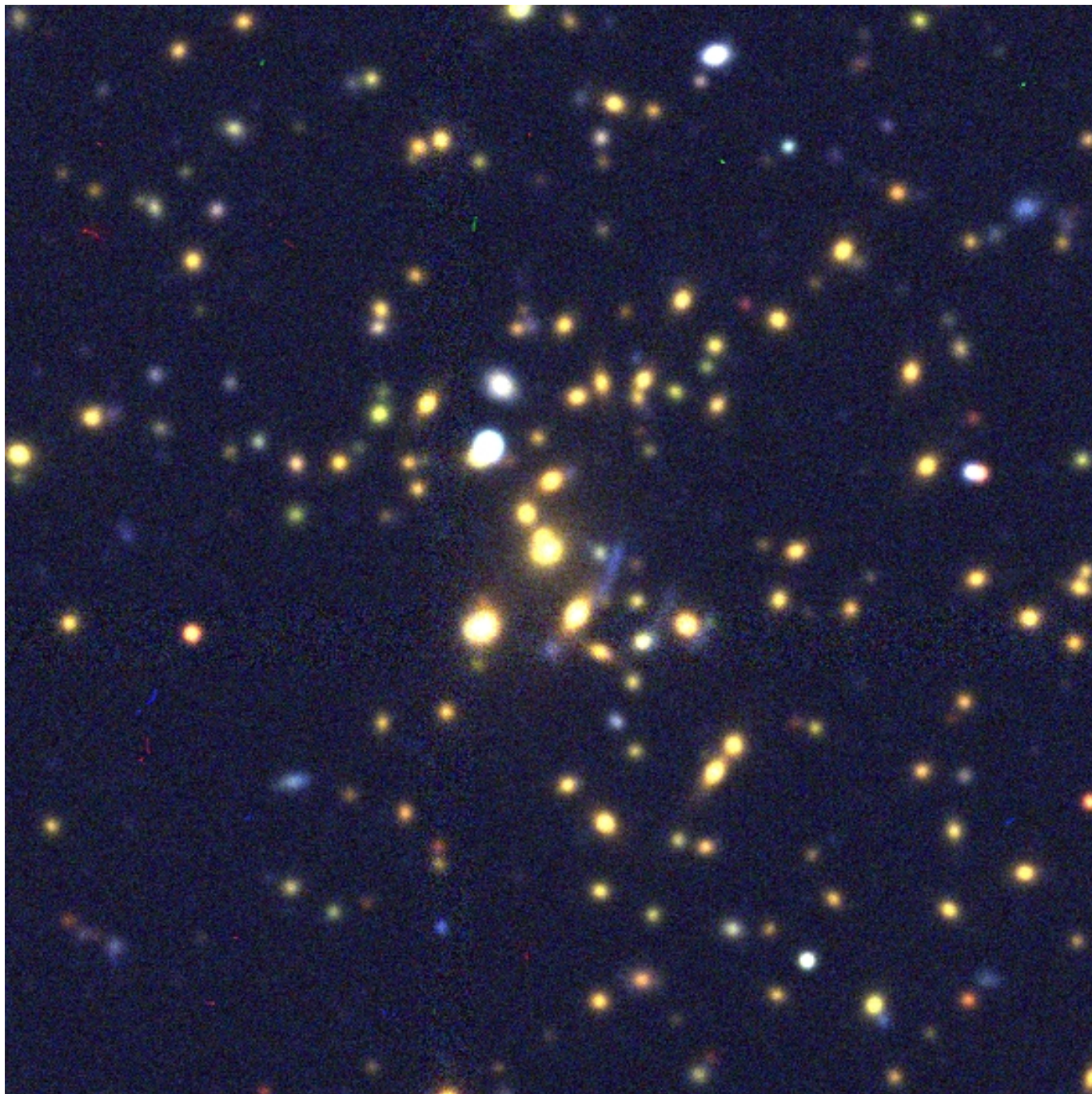


Figure 11. Example CTIO 4 m observed strong lens from the SPT cluster sample, either a simulated or real image.

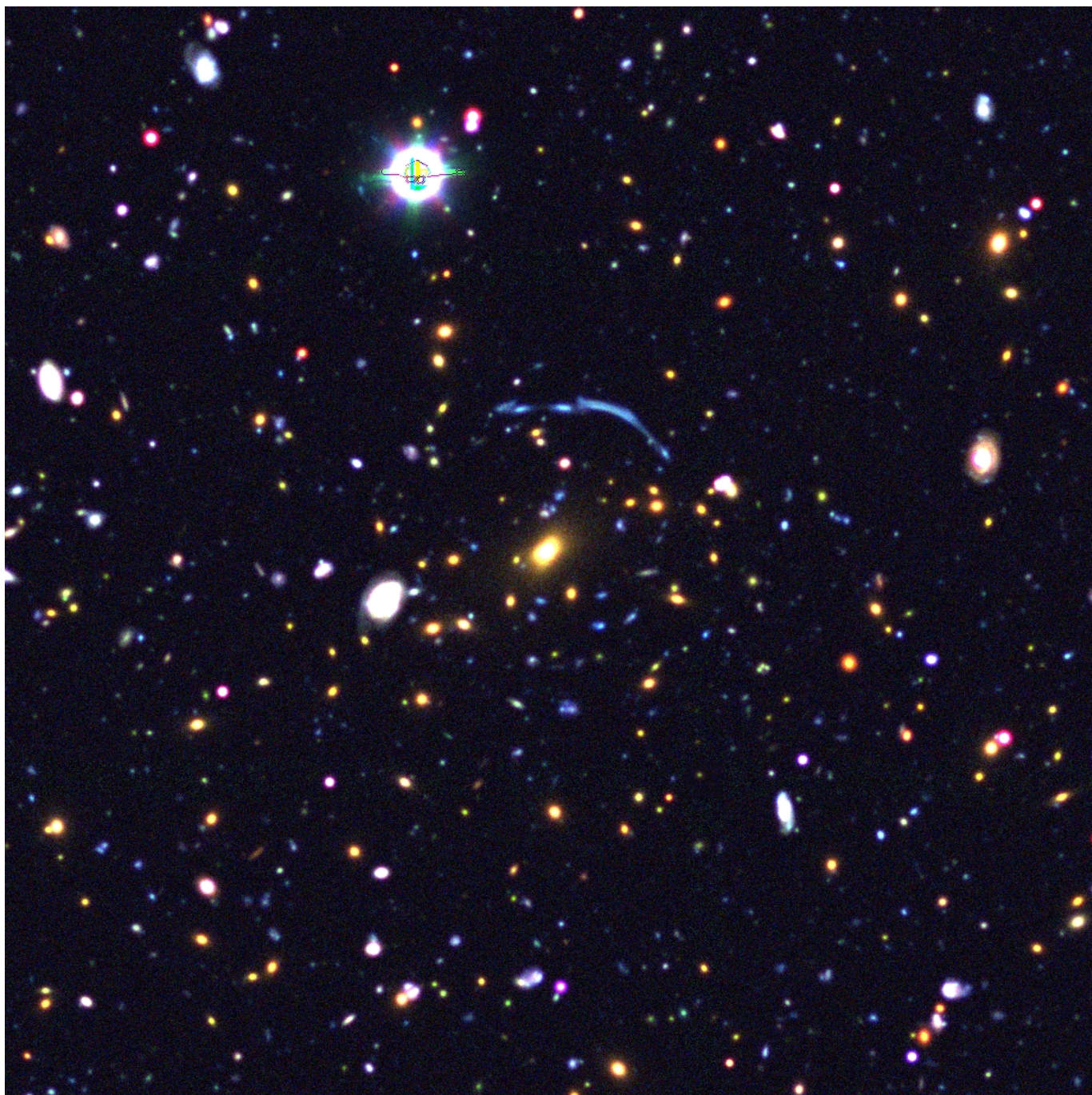


Figure 12. Example Magellan 6.5 m observed strong lens from the SPT cluster sample, either a simulated or real image.



Figure 13. Example Magellan 6.5 m observed strong lens from the SPT cluster sample, either a simulated or real image.